



Strain effects on in-plane conductance of the topological insulator Bi₂Te₃

Jin Heui Hwang, Sangku Kwon, Joonbum Park, Jong Hun Kim, Jinhwan Lee, Jun Sung Kim, Ho-Ki Lyeo, and Jeong Young Park

Citation: *Applied Physics Letters* **104**, 161613 (2014); doi: 10.1063/1.4873389

View online: <http://dx.doi.org/10.1063/1.4873389>

View Table of Contents: <http://scitation.aip.org/content/aip/journal/apl/104/16?ver=pdfcov>

Published by the AIP Publishing

Articles you may be interested in

[Effect of carrier recombination on ultrafast carrier dynamics in thin films of the topological insulator Bi₂Se₃](#)
Appl. Phys. Lett. **105**, 171905 (2014); 10.1063/1.4901052

[Resolving the Dirac cone on the surface of Bi₂Te₃ topological insulator nanowires by field-effect measurements](#)
Appl. Phys. Lett. **104**, 243115 (2014); 10.1063/1.4883887

[Magneto-resistance up to 60 Tesla in topological insulator Bi₂Te₃ thin films](#)
Appl. Phys. Lett. **101**, 202403 (2012); 10.1063/1.4766739

[Topological insulator Bi₂Te₃ films synthesized by metal organic chemical vapor deposition](#)
Appl. Phys. Lett. **101**, 162104 (2012); 10.1063/1.4760226

[Atomic-layer-deposited Al₂O₃ on Bi₂Te₃ for topological insulator field-effect transistors](#)
Appl. Phys. Lett. **99**, 052108 (2011); 10.1063/1.3622306

Not all AFMs are created equal
Asylum Research Cypher™ AFMs
There's no other AFM like Cypher

www.AsylumResearch.com/NoOtherAFMLikeIt

OXFORD
INSTRUMENTS
The Business of Science®

The advertisement features a dark blue background with a film strip graphic on the left. The text is in white and orange. The Oxford Instruments logo is in the bottom right corner.

Strain effects on in-plane conductance of the topological insulator Bi_2Te_3

Jin Heui Hwang,^{1,2} Sangku Kwon,^{1,2} Joonbum Park,³ Jong Hun Kim,^{1,2} Jhinhwan Lee,⁴ Jun Sung Kim,³ Ho-Ki Lyeo,⁵ and Jeong Young Park^{1,2,a)}

¹Center for Nanomaterials and Chemical Reactions, Institute for Basic Science (IBS), Daejeon 305-701, South Korea

²Graduate School of EEWS, Korea Advanced Institute of Science and Technology (KAIST), Daejeon 305-701, South Korea

³Department of Physics, Pohang University of Science and Technology, Pohang 790-784, South Korea

⁴Department of Physics, KAIST, Daejeon 305-701, South Korea

⁵Korea Research Institute of Standards and Science, 267 Gajeong-ro, Yuseong-gu, Daejeon 305-340, South Korea

(Received 10 February 2014; accepted 15 April 2014; published online 25 April 2014)

We investigated the correlation between electrical transport and mechanical stress in a topological insulator, Bi_2Te_3 , using conductive probe atomic force microscopy in an ultrahigh vacuum environment. After directly measuring charge transport on the cleaved Bi_2Te_3 surface, we found that the current density varied with applied load. Current mapping revealed a variation of the current on different terraces. The current density increased in the low-pressure regime and then decreased in the high-pressure regime. This variation of current density was explained in light of the combined effect of changes in the in-plane conductance due to spin-orbit coupling and hexagonal warping. © 2014 AIP Publishing LLC. [<http://dx.doi.org/10.1063/1.4873389>]

Three-dimensional topological insulators (TIs), characterized by a nontrivial Z_2 topology of the bulk wave function, are insulating in the bulk with unusual metallic surface states that consist of spin-polarized Dirac fermions.¹⁻⁴ Surface states of TIs are protected by the spin-orbit interaction and time-reversal symmetry.^{2,4} Such spin-helical states are insensitive to disorder or local perturbations because no states are available for backscattering.^{5,6} Therefore, low energy dissipation can be expected during electron transport processes.^{7,8} Characteristics of electron transport phenomena with low energy loss make a dramatic increase in energy efficiency possible, which is crucial for future energy industries.

Thus far, many attempts have been made to achieve TI-based electronic devices, including using the ambipolar field effect, flexible electrodes, and supercomputers.⁹⁻¹³ During fabrication of electronic devices, stress control is important because of its effect on charge transport properties. Differences in thermal expansion and in the lattice constant between contact materials cause strain that can be avoided. This strain modifies the charge transport at the interface, resulting in stability issues for these devices. While density functional theory calculations demonstrated strain effects on topological states,¹⁴⁻¹⁶ few transport experiments that focus on mechanical deformation have been reported.¹³ Recently, scanning probe microscopy has been widely used to explore the unique characteristics of TIs.¹⁷⁻²² For the most part, atomic force microscopy (AFM) studies have focused on observing surface topography.^{21,23} Due to the nanoscale size of the contact area between the AFM tip and sample, it is possible to investigate nanoscale charge transport without needing complicated processes for the electrodes. Thus, we demonstrate the relationship between charge transport and

nanomechanical properties using conductive probe atomic force microscopy (CP-AFM) in ultrahigh vacuum (UHV).

We used single crystals of Bi_2Te_3 grown via self-flux methods.²⁴ The high-purity elements—Bi(5N) and Te(6N)—were sealed in an evacuated quartz ampoule with a stoichiometry of Bi:Te = 2:3. After the mixture was heated to 850 °C and annealed for two days for homogeneity, the mixture was slowly cooled to 600 °C for a week. To ensure high crystallization, the furnace was kept at 600 °C for one additional week before cooling to ambient temperature. The sample was introduced to the vacuum chamber and cleaved in an ultrahigh vacuum environment. A commercial RHK-Tech UHV AFM system was used for the AFM experiments. To avoid forces originating from capillary water between the tip and the sample at ambient pressure, the chamber was maintained at a base pressure of 1.0×10^{-10} Torr. TiN-coated cantilevers (made by NT-MDT) with a force constant of 0.11 N/m were utilized to measure the conductance and friction. The measurements were performed using a hybrid combination of CP-AFM and friction force microscopy (FFM) for simultaneous detection of atomic-scale forces and conduction properties.²⁵⁻²⁷ Conventional contact mode AFM uses cantilever deflection as the feedback signal to regulate the tip-sample distance. When electrically conductive AFM tips are connected to a current pre-amplifier, the tip-sample current is obtained as an additional independent signal when a bias voltage is applied between the conducting tip and a conductive substrate.²⁶ The radii of the metal-coated tips were 30–50 nm before contact, as measured by scanning electron microscopy. However, when measured after a contact experiment, the radii were found to be 35 ± 10 nm. Because the measured friction force does not show time-dependent behavior during the experiments, we assume that any changes to the tip radius take place soon after the initial contact. The range of stress measured is in the elastic regime with minimal changes

^{a)}Author to whom correspondence should be addressed. Electronic mail: jeongypark@kaist.ac.kr.

during subsequent contact measurements. By analyzing the topographical and frictional images after the contact AFM experiment, we confirm that the loads are sufficiently small such that neither the tip nor the surface was damaged.

Figs. 1(a)–1(c) show $200 \times 200 \text{ nm}^2$ topographic, friction, and current images, respectively. Line profiles of each image in Figs. 1(d)–1(f) reveal steps along the yellow line in Fig. 1(a). An applied load of 8.2 nN and sample bias of 2.0 V were used for the contact mode AFM imaging. We were able to observe atomic steps in most areas of the sample and each step extended from several nanometers to several micrometers. According to the X-ray diffraction study, a single layer of Bi_2Te_3 consists of Te-Bi-Te-Bi-Te with covalent bonds (i.e., a quintuple layer) and each quintuple layer is connected by van der Waals forces.²⁴ The height of a single step is $1.0 \pm 0.2 \text{ nm}$, which implies that the left and right sides of the topography image correspond to single and double quintuple layers, respectively. The friction image in Fig. 1(b) did not provide any differences between one step and another, as shown in the line profile in Fig. 1(e). Friction measurements of the back and forth scanning of the AFM tip produce the red and black lines in the friction image, indicating trace and retrace curves, respectively. Due to weak interbonding and layer composition, we expect the Te atoms to terminate the step terraces. Identical friction between the three different terraces implies that the terraces are chemically equivalent, even though steps separate them.

In contrast to friction on the terraces, the current image in Fig. 1(c) shows three different terraces having distinct conductance. The terrace in the middle of Fig. 1(c) has two clearly distinguishable domains, separated by the black arrow in Fig. 1(a). Differences in conductance between neighboring terraces are not usually observed in normal metallic surfaces (e.g., Au (111)). The variation in current on the terrace can be associated with Bi/Te domains. The self

flux growth of Bi_2Te_3 could contain nonstoichiometric intercalated Bi/Te domains in the van der Waals gap, and a high density of antisite defects exists near the surface layer.²⁸ Indeed, a high internal field may lead to a change in conductance. Also, the density of state of the Bi_2Te_3 can be varied by the internal field and by the level of doping in light of electronic band structures. Liu *et al.* demonstrated the existence of antiphase boundaries between neighboring Bi_2Se_3 grains and that these antiphase boundaries provide electrostatic fields on the order of 10^8 V/m that locally change the Dirac states.²⁹ The internal field modulates the carrier density and shifts the Dirac point by up to 120 meV. We suppose that the different amounts of point defects and defect types generate an internal field between the neighboring terraces, which supports the conductance contrast in Fig. 1(c). Another possibility involves Bi terminal on the Bi_2Te_3 surface.³⁰

Fig. 2(a) shows friction and conductance measured at the center of the terrace on the Bi_2Te_3 surface. The measurements were taken with a 1 V sample bias. The yellow and green points indicate current and friction, respectively. While friction increased moderately as the applied load increased, the current increased and saturated when the normal force exceeded 50 nN. In the wearless regime, friction at a single asperity (f) is described by $f = \tau A$, where A is the contact area and τ is the shear stress at the interface. Thus, we can regard friction as the contact area since shear stress (τ) is not a function of applied load but is a constant value determined by material and surface conditions.³¹ We calculated the contact area using the Derjaguin–Muller–Toporov (DMT) continuum mechanical model.^{32–34} The elastic modulus (E_{BTS}) of 39.6 GPa for Bi_2Te_3 was measured by nanoindentation with a Poisson's ratio (ν_{BTS}) of 0.3. A combined modulus of 40.7 GPa (from $E_{\text{TiN}} = 600 \text{ GPa}$ and $\nu_{\text{BTS}} = 0.25$)²⁵ and tip radius of 35 nm were used for DMT fitting. The adhesion force of $20.1 \pm 0.7 \text{ nN}$ was measured

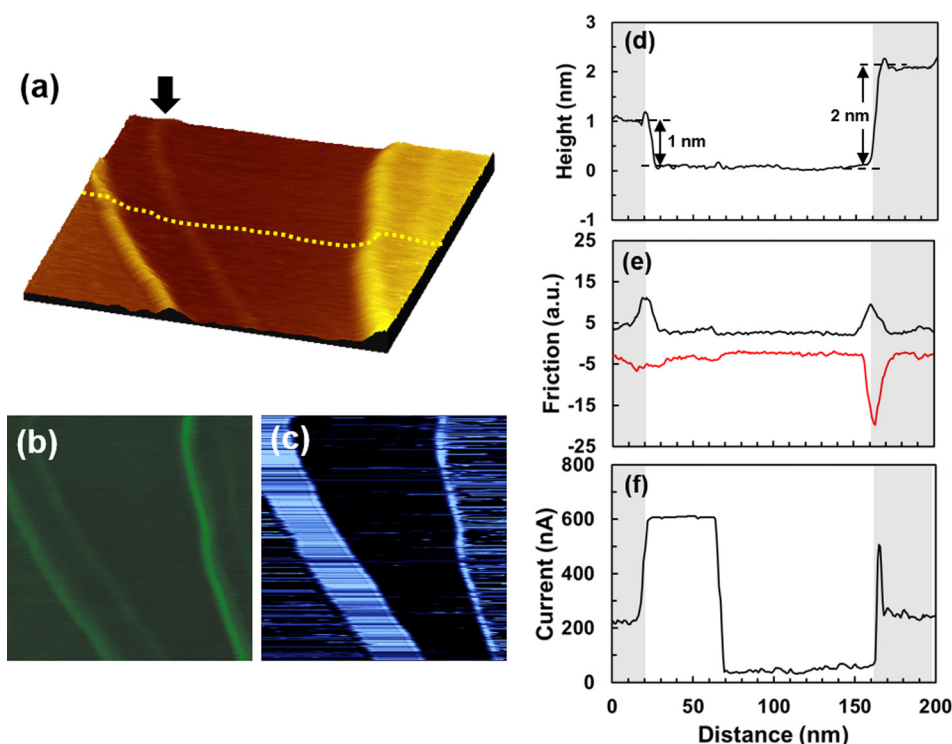


FIG. 1. $200 \times 200 \text{ nm}^2$ images of (a) topography, (b) friction, and (c) current taken using contact mode AFM on the Bi_2Te_3 surface (applied load = 8.2 nN, sample bias = 2 V). Line profiles of (d) topography, (e) friction, and (f) current revealing three neighboring terraces. The trace (red) and retrace (black) curves shown in the friction image (f) are due to back and forth scanning of the AFM tip.

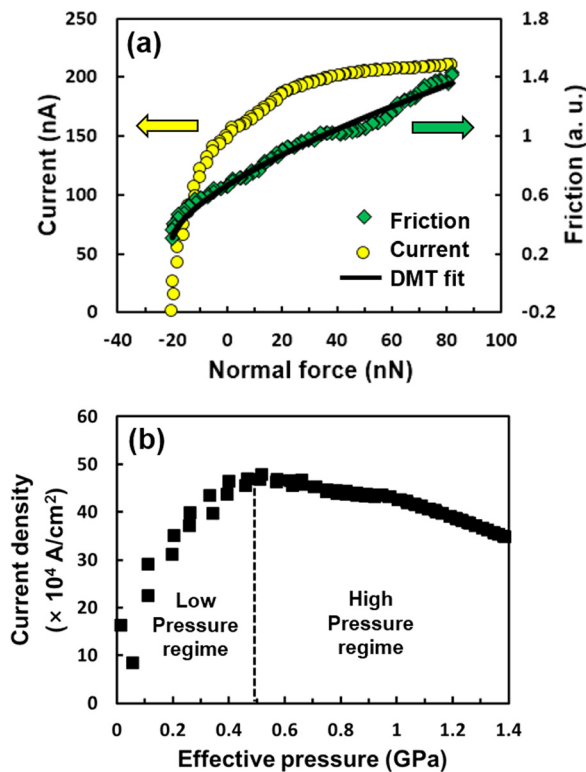


FIG. 2. (a) Current and lateral force as a function of applied load measured on the Bi_2Te_3 surface at a 1 V sample bias. The tip-sample contact area (black line) is fitted using the DMT model. (b) The current density was obtained as a function of effective pressure from (a).

from force–distance curves on the Bi_2Te_3 surface. From the calculated contact area, we obtained current density (A/cm^2) as a function of effective pressure (GPa) after considering the adhesion force, as shown in Fig. 2(b). We identified two regimes in the current density that depend on applied pressure: the low-pressure regime where current density increased, and the high-pressure regime where current density decreased.

We were able to observe crossover behavior of current density in most areas of the sample, but degradation of the current density occurs at various pressures along the different conductive terraces. Two neighboring terraces can be observed in Figs. 3(a) and 3(b): a high-conductive terrace (HCT) and low-conductive terrace (LCT). Current density of the HCT increased rapidly at low pressure, turning to degradation at an effective pressure of 0.2 GPa, but 0.5 GPa is needed before degradation occurs in the LCT. To analyze the unusual behavior of the current density, we separated the components of conductance into the in-plane and out-of-plane directions. Out-of-plane conductance only corresponds to bulk conductance, which is not sensitive to local deformation. Therefore, the surface contribution is significant in atomic-scale conductance because local bending mostly influences the in-plane conductance from the surface states. Each component dominantly influences the conductance in different pressure regimes.

The schematic diagram in Fig. 4(a) displays the physical origin of current density variation with threshold pressure (P_t). At low-pressure ($P < P_t$), the increase in current density is attributed to strain-induced enhancement of the local density of states (LDOS). According to previous first-principle

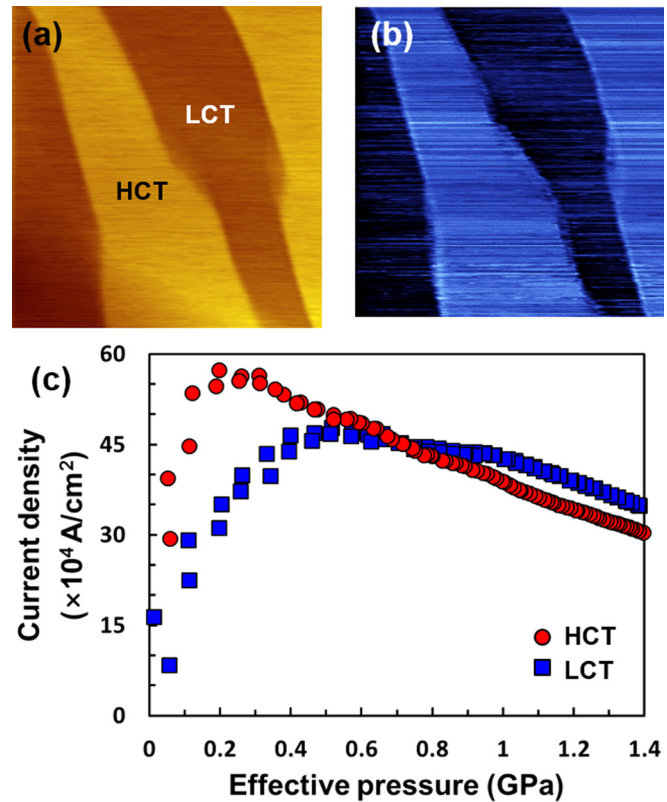


FIG. 3. $200 \times 200 \text{ nm}^2$ images of (a) topography and (b) current taken on the Bi_2Te_3 surface (applied load = 18.7 nN, sample bias = 0.34 V). HCT and LCT represent high-conductive terrace and low-conductive terrace, respectively. (c) Current density was obtained as a function of effective pressure at 0.5 V of sample bias.

calculations, the inverted bulk band is sensitive to uniaxial strain,^{14–16,35} even destroying the topological phase at over 8% deformation due to modification of the Coulomb interaction and spin–orbit coupling.¹⁵ Strain from the AFM tip is localized in a nanosized area; uniaxial strain shifts the band gap near the surface. When a relatively small pressure is applied to the Bi_2Te_3 surface, the tip does not destroy the topological phase on the Bi_2Te_3 surface. Thus, we can attribute the increase in current density to a shift in the surface state.

In the high-pressure regime ($P > P_t$), surface conductance decreases as the strain increases upon loading the tip, which results in a decrease in current density. The robustness of surface states is well known in various circumstances via ARPES measurements and DFT calculations.^{36–38} Their scattering properties, however, can be customized as the chemical potential and band alignment are modified. Near the Dirac point, the energy dispersion has a perfect cone shape and backward scattering is prohibited by the underlying spin texture. However, as the chemical potential approaches the bottom of the conduction bands, the shape of the Fermi surface for the surface state changes from a perfect circle to a rounded hexagon, which is called the hexagonal warping effect, as shown in Fig. 4(b).^{24,39} This leads to distortion of the spin texture, which causes enhanced oblique scattering. Local deformation becomes significant at higher loads and one can expect enhanced hexagonal warping as the chemical potential (with respect to the Dirac point) and band alignment between the topological surface state and the bulk band states are modified. This implies that the reduction in

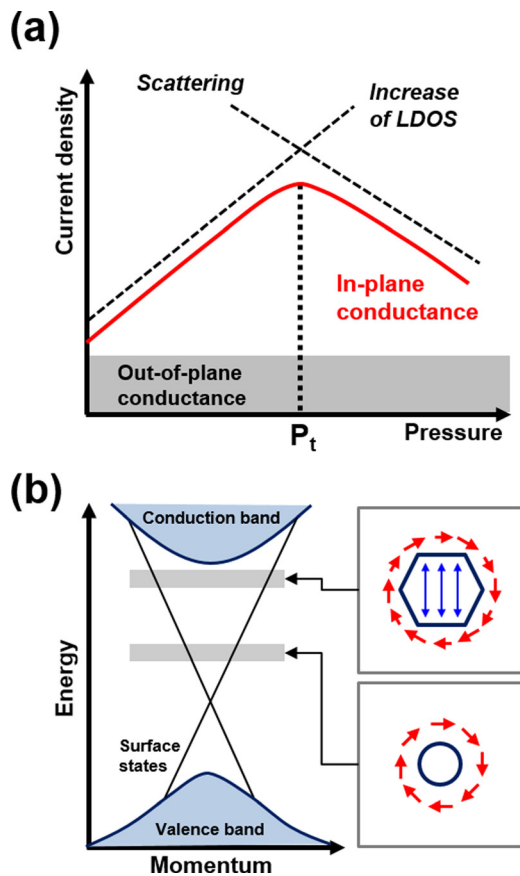


FIG. 4. Schematics of (a) the physical origins of current density crossover on the in-plane conductance and (b) the hexagonal warping effect of the surface states.

current density can be explained in terms of enhanced scattering as a result of hexagonal warping effects in the high-pressure regime. Based on the Hall measurement, we confirmed that our Bi_2Te_3 topological insulator is n-type. The Hall measurement on the Bi_2Te_3 showed a carrier concentration of $7.91 \times 10^{16} \text{ cm}^{-3}$ and a Hall coefficient of $-78.9 \text{ cm}^3/\text{C}$, measured with a probing current of 500 nA. From the low carrier concentration, we expect the Fermi level to be located on the upper side of the Dirac point so it is close enough to sense the band shift in the low-pressure regime, because it has a hexagonal shape in isotropic energy, which is consistent with our observations. In addition to hexagonal warping effects, the two-dimensional electron gas (2DEG) formed by surface band bending and confined in the metallic state also contributes to the scattering process.^{36,38} We were not able to separate scattering components between the 2DEG and hexagonal warping effects in the current study; thus, it remains for future study. We note that other narrow band gap semiconductors (e.g., Si) do not exhibit such pressure dependence.⁴⁰

In conclusion, we studied the influence of mechanical deformation on the charge transport properties of Bi_2Te_3 surfaces using conductive probe AFM under UHV. We observed that the current density increased as the pressure increased in the low-pressure regime; however, the current density decreased by 0%–60% in the high-pressure regime. These results suggest that surface states play a major role in nanoscale charge transport and are correlated with

mechanical deformation at the atomic scale. Crossover behavior of the current density implies that the local density of states and the scattering component are significantly influenced by local strain.

This work was supported by the Institute for Basic Science (IBS), CA1401-04, the SRC Centre for Topological Matter (Grant Nos. 2011-0030787 and 2001-0030785), and the Mid-Career Researcher Program (Grant No. 2012-013838) through the National Research Foundation (NRF), South Korea.

- ¹J. E. Moore, *Nature* **464**, 194 (2010).
- ²M. Z. Hasan and C. L. Kane, *Rev. Mod. Phys.* **82**, 3045 (2010).
- ³J. E. Moore and L. Balents, *Phys. Rev. B* **75**, 121306 (2007).
- ⁴L. Fu and C. L. Kane, *Phys. Rev. B* **76**, 045302 (2007).
- ⁵T. Zhang, P. Cheng, X. Chen, J.-F. Jia, X. Ma, K. He, L. Wang, H. Zhang, X. Dai, Z. Fang *et al.*, *Phys. Rev. Lett.* **103**, 266803 (2009).
- ⁶P. Roushan, J. Seo, C. V. Parker, Y. S. Hor, D. Hsieh, D. Qian, A. Richardella, M. Z. Hasan, R. J. Cava, and A. Yazdani, *Nature* **460**, 1106 (2009).
- ⁷D. S. Kong and Y. Cui, *Nat. Chem.* **3**, 845 (2011).
- ⁸P. Ghaemi, R. S. K. Mong, and J. E. Moore, *Phys. Rev. Lett.* **105**, 166603 (2010).
- ⁹D. S. Kong, Y. Chen, J. J. Cha, Q. Zhang, J. G. Analytis, K. Lai, Z. Liu, S. S. Hong, K. J. Koski, S.-K. Mo *et al.*, *Nat. Nanotechnol.* **6**, 705 (2011).
- ¹⁰Y. Wang, F. Xiu, L. Cheng, L. He, M. Lang, J. Tang, X. Kou, X. Yu, X. Jiang, Z. Chen *et al.*, *Nano Lett.* **12**, 1170 (2012).
- ¹¹B. Sacepe, J. B. Oostinga, J. Li, A. Ubal dini, N. J. G. Couto, E. Giannini, and A. F. Morpurgo, *Nat. Commun.* **2**, 575 (2011).
- ¹²H. Steinberg, D. R. Gardner, Y. S. Lee, and P. Jarillo-Herrero, *Nano Lett.* **10**, 5032 (2010).
- ¹³H. L. Peng, W. H. Dang, J. Cao, Y. L. Chen, W. Wu, W. S. Zheng, H. Li, Z. X. Shen, and Z. F. Liu, *Nat. Chem.* **4**, 281 (2012).
- ¹⁴W. L. Liu, X. Y. Peng, C. Tang, L. Z. Sun, K. W. Zhang, and J. X. Zhong, *Phys. Rev. B* **84**, 245105 (2011).
- ¹⁵S. M. Young, S. Chowdhury, E. J. Walter, E. J. Mele, C. L. Kane, and A. M. Rappe, *Phys. Rev. B* **84**, 085106 (2011).
- ¹⁶L. Zhao, J. W. Liu, P. Z. Tang, and W. H. Duan, *Appl. Phys. Lett.* **100**, 131602 (2012).
- ¹⁷A. K. Mitchell, D. Schuricht, M. Vojta, and L. Fritz, *Phys. Rev. B* **87**, 075430 (2013).
- ¹⁸M. T. Tran and K. S. Kim, *Phys. Rev. B* **82**, 155142 (2010).
- ¹⁹T. Hanaguri, K. Igarashi, M. Kawamura, H. Takagi, and T. Sasagawa, *Phys. Rev. B* **82**, 081305 (2010).
- ²⁰P. Cheng, C. Song, T. Zhang, Y. Zhang, Y. Wang, J.-F. Jia, J. Wang, Y. Wang, B.-F. Zhu, X. Chen *et al.*, *Phys. Rev. Lett.* **105**, 076801 (2010).
- ²¹S. S. Hong, W. Kundhikanjana, J. J. Cha, K. J. Lai, D. S. Kong, S. Meister, M. A. Kelly, Z. X. Shen, and Y. Cui, *Nano Lett.* **10**, 3118 (2010).
- ²²G. L. Hao, X. Qi, Y. D. Liu, Z. Y. Huang, H. X. Li, K. Huang, J. Li, L. W. Yang, and J. X. Zhong, *J. Appl. Phys.* **111**, 114312 (2012).
- ²³G. Koren, T. Kirzhner, E. Lahoud, K. B. Chashka, and A. Kanigel, *Phys. Rev. B* **84**, 224521 (2011).
- ²⁴Y. L. Chen, J. G. Analytis, J.-H. Chu, Z. K. Liu, S.-K. Mo, X. L. Qi, H. J. Zhang, D. H. Lu, X. Dai, Z. Fang *et al.*, *Science* **325**, 178 (2009).
- ²⁵S. Kwon, S. Choi, H. J. Chung, H. Yang, S. Seo, S. H. Jhi, and J. Y. Park, *Appl. Phys. Lett.* **99**, 013110 (2011).
- ²⁶J. Y. Park, S. Maier, B. Hendriksen, and M. Salmeron, *Mater. Today* **13**, 38 (2010).
- ²⁷J. Y. Park, D. F. Ogletree, P. A. Thiel, and M. Salmeron, *Science* **313**, 186 (2006).
- ²⁸F. T. Huang, M. W. Chu, H. H. Kung, W. L. Lee, R. Sankar, S. C. Liou, K. K. Wu, Y. K. Kuo, and F. C. Chou, *Phys. Rev. B* **86**, 081104 (2012).
- ²⁹Y. Liu, Y. Y. Li, D. Gilks, V. K. Lazarov, M. Weinert, and L. Li, *Phys. Rev. Lett.* **110**, 186804 (2013).
- ³⁰P. M. Coelho, G. A. S. Ribeiro, A. Malachias, V. L. Pimentel, W. S. Silva, D. D. Reis, M. S. C. Mazzoni, and R. Magalhaes-Paniago, *Nano Lett.* **13**, 4517 (2013).
- ³¹R. W. Carpick, D. F. Ogletree, and M. Salmeron, *Appl. Phys. Lett.* **70**, 1548 (1997).
- ³²M. Enachescu, R. J. A. van den Oetelaar, R. W. Carpick, D. F. Ogletree, C. F. J. Flipse, and M. Salmeron, *Phys. Rev. Lett.* **81**, 1877 (1998).

- ³³B. V. Derjaguin, V. M. Muller, and Y. P. Toporov, *Prog. Surf. Sci.* **45**, 131 (1994).
- ³⁴J. Y. Park, D. F. Ogletree, M. Salmeron, C. J. Jenks, and P. A. Thiel, *Tribol. Lett.* **17**, 629 (2004).
- ³⁵K. S. Yang, W. Setyawan, S. D. Wang, M. B. Nardelli, and S. Curtarolo, *Nature Mater.* **11**, 614 (2012).
- ³⁶M. Bianchi, D. D. Guan, S. N. Bao, J. L. Mi, B. B. Iversen, P. D. C. King, and P. Hofmann, *Nat. Commun.* **1**, 128 (2010).
- ³⁷M. Koleini, T. Frauenheim, and B. H. Yan, *Phys. Rev. Lett.* **110**, 016403 (2013).
- ³⁸C. Y. Chen, S. He, H. Weng, W. Zhang, L. Zhao, H. Liu, X. Jia, D. Mou, S. Liu, J. He *et al.*, *Proc. Natl. Acad. Sci. U.S.A.* **109**, 3694 (2012).
- ³⁹L. Fu, *Phys. Rev. Lett.* **103**, 266801 (2009).
- ⁴⁰J. Y. Park, R. J. Phaneuf, D. F. Ogletree, and M. Salmeron, *Appl. Phys. Lett.* **86**, 172105 (2005).